The Interplay of Irradiated- and Shaded Zones in Photoreactor Scale-Up

Benedikt Wiedemann[a], Keiran Mc Carogher[b], Simon Kuhn[b], Dirk Ziegenbalg[a*]

[a]Institute of Chemical Engineering, Ulm University, Albert-Einstein-Allee 11, 89081 Ulm, Germany

[b]Department of Chemical Engineering, KU Leuven, Celestijnenlaan 200F, 3001 Leuven, Belgium

Dirk Ziegenbalg - dirk.ziegenbalg@uni-ulm.de

*Corresponding author

Abstract

Despite the potential benefits of using light to drive chemical reactions, photoreactions are rarely implemented on an industrial scale. One of the main issues is the challenging scale-up due to the exponential light attenuation with increasing optical pathlength. Therefore, shaded zones within the reactor can exist at positions far from the light source with few available photons and thus low reactivity. To analyze the impact of light attenuation and to optimize the reaction conditions during scale-up, a compartment model is presented and benchmarked with a photooxidation reaction in a Taylor-flow capillary reactor. The simulation results highlight that a thorough optimization of light intensity and photosensitizer concentration, as well as an enhanced mixing of the liquid phase, are required to minimize the reaction-inhibiting effect of light attenuation and to enable a high reactor performance, especially during scale-up.

Keywords

Upscaling, Photoreactor, Mass transport, Shading, Slug flow, Photooxidation

Latin Symbols

Symbol	Unit	Description
$\boldsymbol{A}$	1	absorbance
$\boldsymbol{A_{cross}}$	m^2	cross-sectional area
$\boldsymbol{c}$	mol m^{-3}	concentration
$\boldsymbol{d}$	m	diameter
$\mathbf{Da_I}$	1	Damkoehler number I
$\mathbf{Da_{II}}$	1	Damkoehler number II
$\boldsymbol{I}$	1	intensification factor
$\boldsymbol{k}$	s^{-1}	reaction rate constant
$\boldsymbol{ka}$	s^{-1}	mass transfer coefficient between irradiated and shaded compartment
$\boldsymbol{l_{irr}}$	m	optical pathlength
$\boldsymbol{\bar{l}_{irr}}$	m	average optical pathlength
$\boldsymbol{L}$	m	length
$\boldsymbol{\dot{n}_{conv}}$	mol s^{-1}	converted molar flux
$\boldsymbol{p}$	Pa	pressure
$\boldsymbol{q}$	mol s^{-1}	photon flux
$\boldsymbol{r}$	mol m^{-3} s^{-1}	reaction rate
$\boldsymbol{R}$	J mol^{-1} K^{-1}	universal gas constant
$\boldsymbol{R^2}$	1	coefficient of determination
$\boldsymbol{t}$	s	time
$\boldsymbol{T}$	K	temperature
$\boldsymbol{u}$	m s^{-1}	velocity

$\bar{\boldsymbol{u}}$	$\mathrm{m\ s^{-1}}$	mean velocity
$\boldsymbol{V}$	$\mathrm{m^3}$	volume
$\dot{\boldsymbol{V}}$	$\mathrm{m^3\ s^{-1}}$	volumetric flow rate
$\boldsymbol{X}$	1	conversion
x	m	radial coordinate
$\boldsymbol{z}$	m	axial coordinate

Greek Symbols

Symbol	Unit	Description
$\boldsymbol{\beta}$	1	gas fraction
$\boldsymbol{\delta}$	m	film thickness
$\boldsymbol{\varepsilon}$	1	void fraction
$\boldsymbol{\varepsilon_{abs}}$	$\mathrm{m^3\ mol^{-1}\ m^{-1}}$	absorption coefficient
$\boldsymbol{\xi}$	1	photonic efficiency
$\boldsymbol{\tau}$	s	residence time
$\boldsymbol{\phi_{\Delta}}$	1	quantum yield

Sub- and Superscripts

Symbol	Description
0	initial
1	scenario 1: constant volumetric photon flux
2	scenario 2: constant irradiance
d	deactivation
film	liquid film

g	gas
in	inlet
irr	irradiated
l	liquid
max	maximum
MT	radial mass transport
O2	oxygen
out	outlet
PS	photosensitizer
r	reaction
ref	reference
R	reactor
s	superficial
sat	saturation
shad	shaded

Abbreviations

Symbol	Description
DMA	9,10-dimethylanthracene
LED	light emitting diode
RB	rose bengal

1 Introduction

In 2022, 86 % of the worldwide primary energy was produced from oil, coal, natural gas, or uranium [1]. In addition, the world energy consumption is projected to increase by 47 % from 2020 to 2050 due to economic growth and increasing world population [2]. Considering the limited availability of fossil resources and the high associated greenhouse gas emissions, it is therefore essential to focus on renewable energy sources in the future [3]. In particular, solar irradiation has great potential, as its use does not create a negative ecological footprint and it is abundantly available. The solar energy reaching the earth's surface within 80 min is equal to the human energy demand of an entire year [4].

Despite the advantages of utilizing light, there is currently only a small number of industrial applications of light-driven reactions [5]. One of the main reasons is the challenging scale-up of photoreactors, since additional radiation constraints must be considered in addition to the molecular constraints in thermal reactions [6,7]. A simple increase in reactor dimensions is not feasible because the light intensity attenuates exponentially with optical pathlength according to the Beer-Lambert law shown in equation (1). The absorbance A and thus the amount of available photons decays exponentially over the optical pathlength l_{irr}, depending on the absorption coefficient $\varepsilon_{\mathrm{abs}}$ of the reaction solution and the concentration of the photoactive substance c.

$$A = \varepsilon_{\mathrm{abs}} c l_{\mathrm{irr}} \tag{1}$$

Due to the light attenuation, sophisticated reactor concepts are required to maintain a high selectivity and productivity during up-scaling [5]. Several concepts are proposed in recent literature to enable efficient photoreactor scale-up, *e.g.*, spinning disk reactors [8], Taylor-Couette reactors [9], falling film reactors [10], or the use of static mixers [11].

In particular for gas-liquid photoreactions, Taylor-flow capillary reactors have been widely studied [12–18]. As illustrated in Fig. 1, the Taylor-flow regime is characterized by alternating segments of liquid slugs and gas bubbles, which are separated from the reactor wall by a thin liquid film. These flow conditions provide a large interfacial area, near

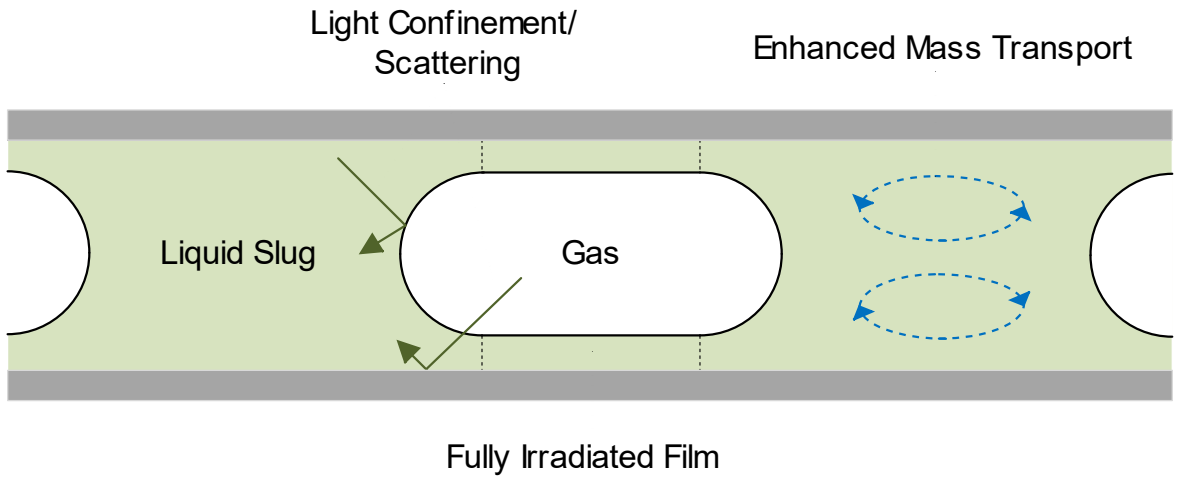

Fig. 1: Overview of a Taylor-flow reactor and explanations in literature for an increased substrate conversion compared to single-phase flow.

plug flow behavior and short diffusion distances [19,20]. In the context of photoreactions, a high reaction rate in the thin liquid film, increasing light confinement and scattering effects, as well as an enhanced liquid sided mass transfer are additional advantages of Taylor-flow reactors [12,13,15]. These effects are illustrated in in Fig. 1.

Nakano et al. studied an organic Paternò-Büchi reaction in a microreactor [13]. By supplying water to the reactor and creating Taylor-flow conditions, the substrate conversion was increased by 70 % at an inlet flow ratio of 1:1 of organic and aqueous phase compared to single-phase flow. Telmesani et al. studied the [2+2]-photocycloaddition of cinnamates using ethyl-acetate as solvent [14]. In single-phase flow, the substrate conversion was limited to 6 %. The addition of water and the corresponding promotion of Taylor-flow increased the conversion to 43 %. As benchmark reaction, photooxidations are commonly used to investigate the performance of photoreactors [21–23]. Potential applications are the synthesis of organic compounds, photo-dynamic anti-cancer therapy, or disinfection [24,25]. Many researchers highlight the increase in substrate conversion in photooxidations under Taylor-flow conditions compared to single phase flow [12–16].

Common explanations for the increased conversion under Taylor-flow conditions and also in other sophisticated reactor concepts like spinning disks or falling films are a small optical path length and an enhanced internal mixing of the liquid phase [8,10–13,15]. To verify this hypothesis, a photoreactor model is proposed in this work to investigate light attenuation and internal mass transport limitations in the liquid phase. The model implications on the reactor performance are discussed using a photooxidation in a Taylor flow

capillary reactor as a reference case. From the simulation results, the role of liquid mixing and light attenuation is investigated, especially during scale-up of a photoreactor. In addition, conclusions are drawn for the selection of photosensitizer concentration and incident photon flux in an upscaled reactor.

2 Material and Methods

2.1 Model for Homogeneous Conditions

Fig. 2 shows a schematic overview of the model approach under homogeneous conditions, *i.e.,* if only a liquid phase is considered. A steady-state, isothermal tubular reactor is assumed which is irradiated by collimated light. Scattering and reflection are assumed to have a negligible effect on the reaction.

The reactor is divided into an irradiated compartment in which reaction takes place and a shaded compartment without reaction. Radial mass transport between both compartments is considered as a diffusion-like process. Within the reactor, a constant liquid volumetric flow rate and plug flow behavior are assumed. The plug flow assumption is validated in Appendix A. Balancing the irradiated volume element $\mathrm{d}V_{\mathrm{irr}}$ and the shaded volume element $\mathrm{d}V_{\mathrm{shad}}$ in Fig. 2 b), leads to equations (2) and (3).

$$-u_{\mathrm{l}}\frac{\mathrm{d}c_{\mathrm{irr}}}{\mathrm{d}z}+ka(c_{\mathrm{shad}}-c_{\mathrm{irr}})\cdot\frac{\mathrm{d}V}{\mathrm{d}V_{\mathrm{irr}}}-r_{\mathrm{irr}}=0 \tag{2}$$

$$-u_{\mathrm{l}}\frac{\mathrm{d}c_{\mathrm{shad}}}{\mathrm{d}z}-ka(c_{\mathrm{shad}}-c_{\mathrm{irr}})\cdot\frac{\mathrm{d}V}{\mathrm{d}V_{\mathrm{shad}}}=0 \tag{3}$$

c_{irr} and c_{shad} represent the DMA concentration at axial position z, in the irradiated compartment and in the shaded compartment, respectively. r_{irr} describes the reaction rate in the irradiated compartment and ka is the mass transfer coefficient between irradiated- and shaded compartment. Therefore, it is not a "traditional" mass transfer coefficient that describes mass transport between different phases. Instead, ka represents the exchange rate of molecules between the two compartments of the liquid phase.

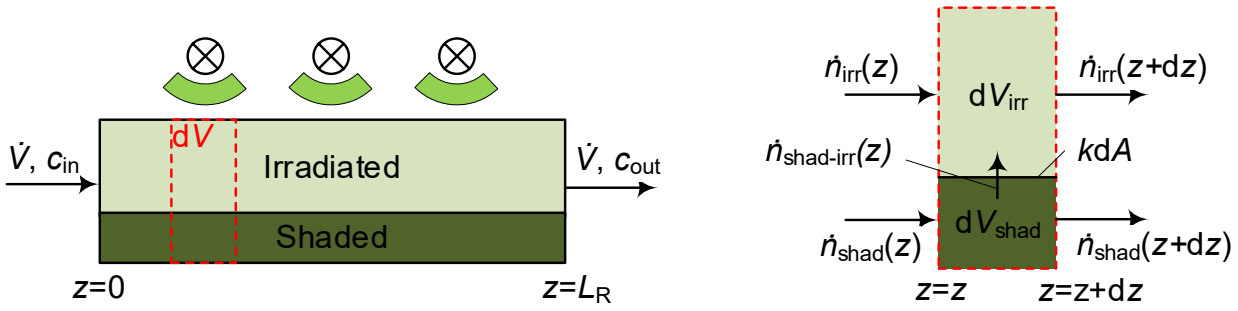

a) Overall Reactor b) Volume Element dV

Fig. 2: Schematic overview of the reactor model for homogeneous conditions.

The liquid velocity u_l is calculated based on the reactor cross-sectional area A_cross and the liquid volumetric flow rate $\dot{V}_\mathrm{l}$ according to equation (4).

$$u_\mathrm{l} = \frac{\dot{V}_\mathrm{l}}{A_\mathrm{cross}} \tag{4}$$

$\mathrm{d}V_\mathrm{irr}$ is approximated by the ratio of optical pathlength l_irr and reactor diameter d_R multiplied by the element volume $\mathrm{d}V$. $\mathrm{d}V_\mathrm{shad}$ equals the difference between $\mathrm{d}V$ and $\mathrm{d}V_\mathrm{irr}$.

$$\mathrm{d}V_\mathrm{irr} = \frac{l_\mathrm{irr}}{d_\mathrm{R}} \cdot \mathrm{d}V \tag{5}$$

$$\mathrm{d}V_\mathrm{shad} = \mathrm{d}V - \mathrm{d}V_\mathrm{irr} = \left(1 - \frac{l_\mathrm{irr}}{d_\mathrm{R}}\right)\mathrm{d}V \tag{6}$$

The optical pathlength is calculated by equation (7). l_irr is estimated as the optical pathlength at which the light intensity reaches 1 % of the initial intensity according to Beer-Lambert law. If the calculated optical pathlength is larger than d_R, $l_\mathrm{irr} = d_\mathrm{R}$ is used instead.

$$l_\mathrm{irr} = \min\left(\frac{-\log_{10}(0.01)}{\varepsilon_\mathrm{abs,PS}\, c_\mathrm{PS}}, d_\mathrm{R}\right) \tag{7}$$

$\varepsilon_\mathrm{abs,\,PS}$ and c_PS are the molar absorption coefficient and the concentration of the photosensitizer, respectively. A validation of the values chosen in equation (7) is provided in Appendix B.

2.2 Model for Heterogeneous Conditions

In addition to the assumptions made in Section 2.1, the two-phase reactor is assumed to be operated under isobaric conditions and a reaction is only considered in the liquid phase but not in the gas phase. The reactor is modeled as an alternating sequence of liquid slugs and oxygen bubbles surrounded by a thin liquid film. A schematic overview is shown in Fig. 3. The liquid phase is considered to be incompressible and the gas to be an ideal gas. Furthermore, it is assumed that oxygen diffuses into the liquid without mass transfer limitations, *i.e.*, the liquid is immediately fully saturated with oxygen at the entrance of the reactor. This assumption is in agreement with very high gas-liquid mass transfer coefficients of up to 21 s^{-1} reported in literature if microchannel reactors are used [26].

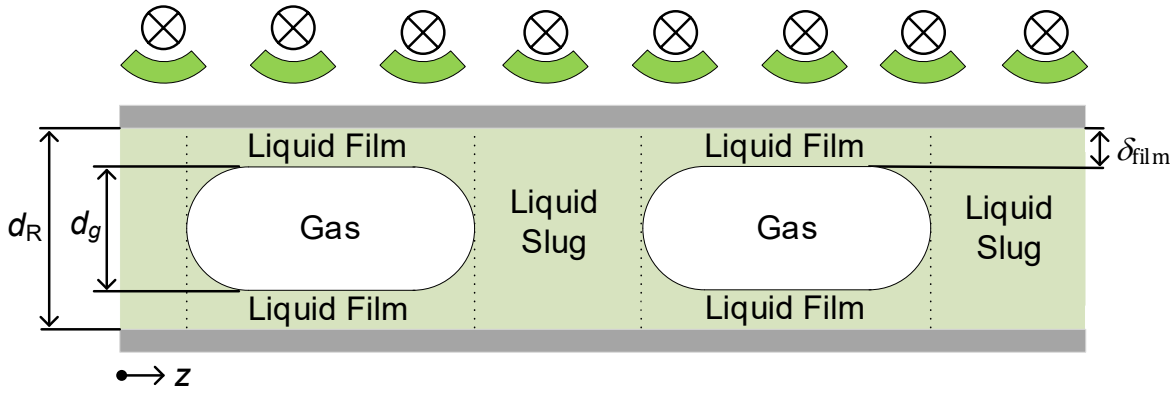

Fig. 3: Schematic overview of the reactor model approach under heterogeneous conditions.

In the liquid film, no shading is considered due to its small thickness. In addition, no mass transport to the slug is assumed due to the small contact area between the film and the slug. The slug is separated into an irradiated and a shaded compartment as described in Section 2.1.

Using the same derivation approach as in Section 2.1, a mass balance of the irradiated part of the slug (index "irr"), its shaded part (index "shad"), and the film (index "film"), results in equations (8)-(10) for the substrate. Note that the liquid velocity u_l decreases over the axial coordinate, since the gas flow rate reduces due to diffusion of the gas into the liquid phase, *i.e.*, $\partial u_l / \partial z \neq 0$.

$$-u_l \frac{\partial c_{irr}}{\partial z} - c_{irr} \frac{\partial u_l}{\partial z} + ka(c_{shad} - c_{irr}) \cdot \frac{dV}{dV_{irr}} - r_{irr} = 0 \quad (8)$$

$$-u_l \frac{\partial c_{shad}}{\partial z} - c_{shad} \frac{\partial u_l}{\partial z} - ka(c_{shad} - c_{irr}) \cdot \frac{dV}{dV_{shad}} = 0 \quad (9)$$

$$-u_l \frac{\partial c_{film}}{\partial z} - c_{film} \frac{\partial u_l}{\partial z} - r_{film} = 0 \quad (10)$$

In Taylor-flow, the velocity of the gas- and the liquid phase is not identical due to the presence of the liquid film [27–30]. Therefore, the void fraction ε differs from the ratio of the inlet volumetric flow rates of gas and liquid [15]. ε represents the ratio of the superficial gas velocity $u_{g,s}$ and the gas velocity in two phase flow u_g. The superficial gas velocity is determined by equation (12).

$$\varepsilon = \frac{u_{\mathrm{g,s}}}{u_{\mathrm{g}}} \tag{11}$$

$$u_{\mathrm{g,s}} = \frac{\dot{V}_{\mathrm{g}}}{A_{\mathrm{cross}}} \tag{12}$$

The liquid velocity u_{l} depends on ε according to equation (13). The superficial liquid velocity $u_{\mathrm{l,s}}$ is calculated by equation (14) using the volumetric flow rate at the reactor inlet $\dot{V}_{\mathrm{in}}$ and the inlet gas fraction β_{g}.

$$u_{\mathrm{l}} = \frac{u_{\mathrm{l,s}}}{(1-\varepsilon)} \tag{13}$$

$$u_{\mathrm{l,s}} = (1-\beta_{\mathrm{g}})\frac{\dot{V}_{\mathrm{in}}}{A_{\mathrm{cross}}} \tag{14}$$

The gas flow rate $\dot{V}_{\mathrm{g}}$ is determined by a material balance of a gas bubble applying the ideal gas law. At $z = 0$, oxygen instantaneously diffuses into the liquid until the saturation concentration of the solvent $c_{\mathrm{O2,sat}}$ is reached, since no gas-liquid mass transport limitations are assumed. Therefore, $\dot{V}_{\mathrm{g}}(z=0)$ is smaller than $\dot{V}_{\mathrm{in}}$ according to equation (15). At $z > 0$, the amount of oxygen absorbed by the liquid equals the converted amount in the film and in the irradiated compartment which leads to equation (16). R is the universal gas constant, T the gas temperature, and p the pressure in the system.

$$\dot{V}_{\mathrm{g}}(z=0) = \left(\beta_{\mathrm{g}} - \frac{RT}{p}\cdot c_{\mathrm{O2,sat}}(1-\beta_{\mathrm{g}})\right)\dot{V}_{\mathrm{in}} \tag{15}$$

$$-\frac{d\dot{V}_{\mathrm{g}}}{dz} - (r_{\mathrm{irr}}\mathrm{d}V_{\mathrm{irr}} + r_{\mathrm{film}}\mathrm{d}V_{\mathrm{film}})\frac{RT}{p} = 0 \tag{16}$$

The volume element occupied by the film $\mathrm{d}V_{\mathrm{film}}$ is approximated by a hollow cylinder. It is calculated by equation (17). The diameter of the gas bubble d_{g} equals the difference between the reactor diameter and two times the film thickness δ_{film}.

$$\mathrm{d}V_{\mathrm{film}} = \frac{\left(d_R^2 - d_{\mathrm{g}}^2\right)}{4}\pi\cdot\mathrm{d}z \tag{17}$$

$$d_{\mathrm{g}} = d_{\mathrm{R}} - 2\delta_{\mathrm{film}} \tag{18}$$

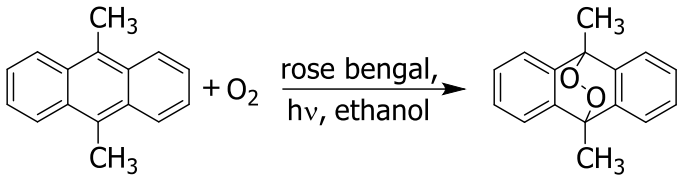

9,10-dimethylanthracene (DMA) DMA endoperoxide

Fig. 4: Benchmark reaction for the model development.

2.3 Benchmark Case and Performance Metrics

The model is implemented with Python using the photooxidation of 9,10-dimethylanthracene (DMA) photosensitized by rose bengal (RB) and dissolved in ethanol ($c_{O2,sat} = 9.8$ mM [31]) as an example reaction. The corresponding reaction scheme is shown in Fig. 4. The model parameterization of the base case for the simulation is aligned with the experimental work conducted by Roibu et al. [16] and summarized in Table 1.

Table 1: Parameters used in the simulation.

Variable	**Unit**	**Studied parameter range in literature**[14]	**Base case in this work**
reactor length	m	0.7	0.7
inner reactor diameter	mm	1	1
DMA inlet concentration	mol m^{-3}	0.24	0.24
temperature	K	298	298
pressure	bar	1	1
RB concentration	mol m^{-3}	$0 - 0.6$	0.6
inlet flow rate	mL min^{-1}	$0.5 - 1.3$	1
bubble velocity	cm s^{-1}	$1.2 - 3.1$	2.34
gas fraction	1	$0 - 0.75$	0.5
incident volumetric photon flux	mmol m^{-3} s^{-1}	$54 - 155$	50
film thickness	µm	$28 - 29$	28

The reaction kinetics model for the photooxidation of DMA is taken from Roibu et al. [16]. The reaction rate in the irradiated compartment and in the liquid film are calculated by equations (19) and (20), respectively.

$$r_{\mathrm{irr}} = \frac{k_{\mathrm{r}}}{k_{\mathrm{d}}} \frac{q_{\mathrm{abs}}}{V} \phi_{\Delta} \cdot c_{\mathrm{irr}} = k c_{\mathrm{irr}} \tag{19}$$

$$r_{\mathrm{film}} = \frac{k_{\mathrm{r}}}{k_{\mathrm{d}}} \frac{q_{\mathrm{abs}}}{V} \phi_{\Delta} \cdot c_{\mathrm{film}} = k c_{\mathrm{film}} \tag{20}$$

k_{r} is the rate constant of singlet oxygen quenching by DMA, and k_{d} is the rate constant of singlet oxygen quenching by the solvent. According to Usui et al. [32], the rate constants are equal to $k_{\mathrm{r}} = 3.9 \cdot 10^{7}\ \mathrm{M^{-1}\ s^{-1}}$ and $k_{\mathrm{d}} = 8.3 \cdot 10^{4}\ \mathrm{s^{-1}}$. The quantum yield ϕ_{Δ} is reported as 0.57 [16]. $q_{\mathrm{abs}}\, V^{-1}$ is the volumetric absorbed photon flux. $k_{\mathrm{r}}, k_{\mathrm{d}}, \phi_{\Delta}$ and $q_{\mathrm{abs}}\, V^{-1}$ are summarized in the reaction rate constant k.

Roibu et al. determined the volumetric absorbed photon flux within the entire reactor volume $q_{\mathrm{abs}}\, V_{\mathrm{tot}}^{-1}$ by actinometric measurements and equation (21). $\bar{l}_{\mathrm{irr}}$ describes the average optical pathlength which is reported as 0.8 mm [16]. The molar absorption coefficient $\varepsilon_{\mathrm{abs,PS}}$ equals 42549 $\mathrm{M^{-1}\ cm^{-1}}$ and the received volumetric photon flux $q_0\, V_{\mathrm{tot}}^{-1}$ is 54.9 mmol $\mathrm{m^{-3}\ s^{-1}}$ at an electrical driving current of 1.77 mA per LED[16]. Since the used current per LED is varied in the work of Roibu et al. but only the corresponding incident photon flux for a current of 1.77 mA is reported, $\mathrm{q_0}\, V_{\mathrm{tot}}^{-1}$ is assumed to increase linearly with the electrical current.

$$\frac{q_{\mathrm{abs}}}{V_{\mathrm{tot}}} = \frac{q_0}{V_{\mathrm{tot}}} \left(1 - 10^{-\varepsilon_{\mathrm{abs,PS}} c_{\mathrm{PS}} \bar{l}_{\mathrm{irr}}}\right) \tag{21}$$

As the entire amount of photons is assumed to be absorbed in the irradiated part of the reactor, $q_{\mathrm{abs}}\, V^{-1}$ is calculated by equation (22).

$$\frac{q_{\mathrm{abs}}}{V} = \frac{q_{\mathrm{abs}}}{V_{\mathrm{tot}}} \frac{d_{\mathrm{R}}}{l_{\mathrm{irr}}} \tag{22}$$

Based on equations (2)-(22), the predicted DMA conversion X and the photonic efficiency ξ are calculated using equations (23)-(30) to study the performance of the reactor. c_{in} is the overall inlet concentration at $z = 0$, c_{out} is the overall concentration at the reactor outlet $z = L_{\mathrm{R}}$, and $\dot{n}_{\mathrm{conv}}$ describes the converted DMA molar flux between $z = 0$ and $z = L_{\mathrm{R}}$. The ordinary differential equations are solved using a RADAU solver with 100

discretization intervals along the z −direction[33]. As initial concentration, c_{in} is used within all compartments at the reactor inlet at $z = 0$.

$$X = \frac{c_{\mathrm{in}} - c_{\mathrm{out}}}{c_{\mathrm{in}}} \tag{23}$$

$$c_{\mathrm{out}} = \frac{c_{\mathrm{irr}}(z = L_{\mathrm{R}}) \cdot \mathrm{d}V_{\mathrm{irr}} + c_{\mathrm{shad}}(z = L_{\mathrm{R}}) \cdot \mathrm{d}V_{\mathrm{shad}} + c_{\mathrm{film}}(z = L_{\mathrm{R}}) \cdot \mathrm{d}V_{\mathrm{film}}}{\mathrm{d}V_{\mathrm{irr}} + \mathrm{d}V_{\mathrm{shad}} + \mathrm{d}V_{\mathrm{film}}} \tag{24}$$

$$\xi = \frac{\dot{n}_{\mathrm{conv}}}{q_0} = \frac{X c_{\mathrm{in}} \dot{V}_{\mathrm{in}}}{q_0} \tag{25}$$

For reactor scale-up, two scenarios are investigated. In both cases, the tube diameter is increased and the inlet flow rate is adjusted by equation (26) to keep the residence time in the reactor constant. The index "ref" indicates the reference values taken from Table 1.

$$\dot{V}_{\mathrm{in}}(d_R) = \dot{V}_{\mathrm{in,ref}} \frac{d_{\mathrm{R}}^2}{d_{\mathrm{R,ref}}^2} \tag{26}$$

In the first scenario (index "1"), the incident photon flux is scaled with increasing reactor volume, so that $\mathrm{q}_0\, V_{\mathrm{tot}}^{-1}$ is constant. Hence, the correlation between conversion and photonic efficiency is linear according to equation (27). In the second scenario (index "2"), the initial irradiance of the light source I_0 is kept constant. I_0 is known for characterized light sources[34]. Assuming that one half of the reactor surface is irradiated, q_0 and ξ are determined by equations (28) and (29).

$$\xi_1(d_{\mathrm{R}}) = X_1(d_{\mathrm{R}}) \frac{V_{\mathrm{tot}}}{q_{0,1}} \frac{c_{\mathrm{in}} \dot{V}_{\mathrm{in,ref}}}{V_{\mathrm{tot,ref}}} \tag{27}$$

$$q_{0,2} = I_0 \frac{d_R}{2} \pi L_R \tag{28}$$

$$\xi_2(d_{\mathrm{R}}) = X_2(d_{\mathrm{R}}) \frac{2 c_{\mathrm{in}} \dot{V}_{\mathrm{in,ref}}\, d_{\mathrm{R}}}{I_0 V_{\mathrm{tot,ref}}} \tag{29}$$

To analyze the impact of liquid sided mass transport, the intensification factor I and the Damkoehler numbers $\mathrm{Da_I}$ and $\mathrm{Da_{II}}$ are introduced by equations (30)-(32). I represents the ratio of the converted amount of educt if mass transport between the irradiated- and the shaded compartment is included and the converted amount of educt if no mass

transport is considered. Da_I and Da_{II} relate the liquid residence time τ_l or the characteristic time of radial mass transport t_{MT}, respectively, to the characteristic time of reaction t_r[35].

$$I(ka) = \frac{\dot{n}_{conv}(ka)}{\dot{n}_{conv}(ka = 0)} = \frac{X(ka)}{X(ka = 0)} \tag{30}$$

$$Da_I = \frac{\tau_l}{t_r} = k \int_0^{L_R} \frac{1}{u_l} dz \tag{31}$$

$$Da_{II} = \frac{t_{MT}}{t_r} = \frac{k}{ka} \tag{32}$$

3 Results and Discussion

In addition to the experimental work, Roibu et al. proposed a model to predict the DMA conversion in the used capillary reactor [16]. Although it is in good agreement to the experimental data, the model has two major limitations: The experimental conversions are overestimated at high sensitizer concentrations and high incident photon flux. Furthermore, the influence of the gas fraction strongly depends on an empirical factor. Both aspects limit the extrapolability of the model.

In contrast to the approach of Roibu et al., the model developed in this work additionally considers internal mass transport limitations in the liquid phase. The mass transfer coefficient between shaded and irradiated compartment is fitted for each gas fraction to minimize the deviation between simulated and experimental conversion. The obtained ka-values are listed in Table 2. A comparison of the simulated DMA conversion with the experimental data is illustrated in Fig. 5. Over the entire parameter range, the simulated- and the experimental results are in good agreement with a coefficient of determination of $R^2 = 97.2\,\%$ under homogeneous conditions and $R^2 = 98.4\,\%$ under heterogeneous conditions, indicating a high prediction capability over a wide range of flow rates, gas fractions, volumetric photon fluxes, and linear absorption coefficients.

According to the Beer-Lambert law, the incident photon flux and the linear absorption coefficient $\varepsilon_{\mathrm{abs,PS}} c_{\mathrm{PS}}$ determine the amount of absorbed photons and thus the reaction rate. The interplay of both variables and the mass transport coefficient is visualized in Fig. 6. In Fig. 6 a) the volumetric incident photon flux is varied at a constant linear absorption coefficient. At an incident volumetric photon flux of 50 mmol $\mathrm{m^{-3}\ s^{-1}}$, mass transport has

Table 2: Mass transfer coefficient at which the maximum model accuracy to the experimental data for each gas fraction is reached.

$\boldsymbol{\beta_G}$ / **1**	**0**	**0.25**	**0.5**	**0.75**
ka / $\mathrm{s^{-1}}$	0	$6.37 \cdot 10^{-3}$	$2.36 \cdot 10^{-2}$	∞

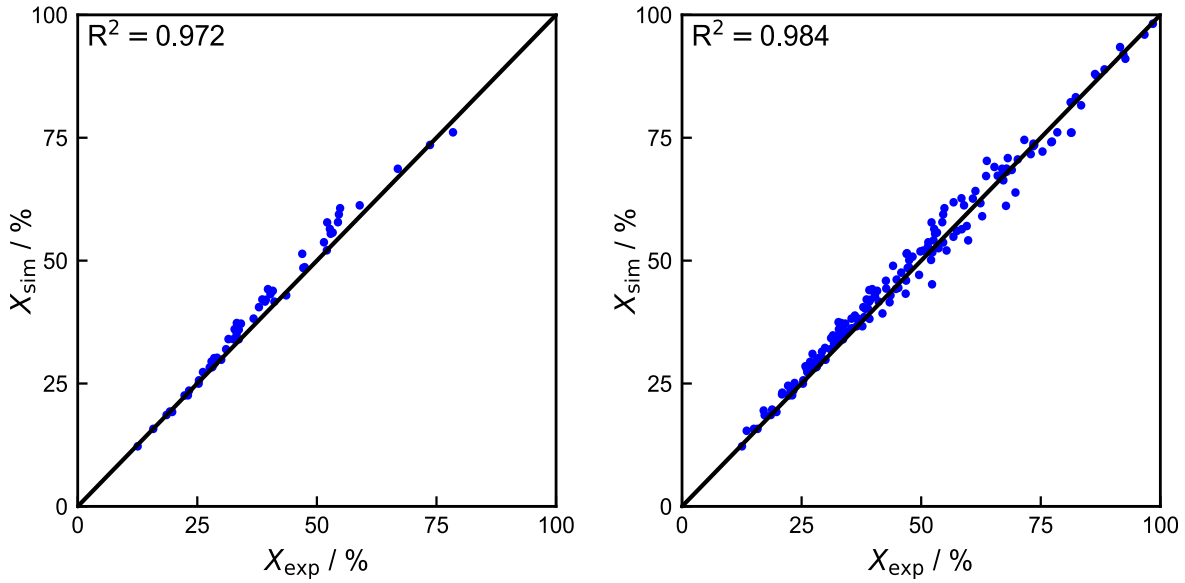

a) Homogeneous conditions b) Heterogeneous conditions

Fig. 5: Comparison of the simulated DMA conversion with experimental data reported by Roibu et al.[14].

only a small impact on the conversion, as the reaction rate is mainly limited photonically. From point A ($ka = 0\ \mathrm{s}^{-1}$) to point B ($ka = 0.1\ \mathrm{s}^{-1}$), the conversion increases from 42.1 % to 44.6 %. With increasing $q_0\ V_{\mathrm{tot}}^{-1}$, the influence of ka on the conversion increases since more DMA is consumed in the irradiated compartment. At $q_0\ V_{\mathrm{tot}}^{-1} = 150\ \mathrm{mmol\ m^{-3}\ s^{-1}}$, the conversion increases from 71.8 % to 82.5 % from point C ($ka = 0\ \mathrm{s}^{-1}$) to point D ($ka = 0.1\ \mathrm{s}^{-1}$).

Fig. 6 b) shows the conversion of DMA as a function of the mass transfer coefficient and increasing $\varepsilon_{\mathrm{abs,PS}} c_{\mathrm{PS}}$. At $ka = 0$, there is a maximum in X at $\varepsilon_{\mathrm{abs,PS}} c_{\mathrm{PS}} = 2011\ \mathrm{m^{-1}}$. Below that value, the reaction rate is too small to reach a high conversion in the irradiated compartment of the reactor. Beyond that value, a high conversion in the irradiated compartment is reached, but according to equation (7) , its volume is shrinking so that the overall conversion within the reactor is decreasing. With increasing ka, the DMA conversion is increasing as more DMA is transferred from the shaded part of the reactor to the irradiated part. In addition, the position of the maximum is shifted to higher values of $\varepsilon_{\mathrm{abs,PS}} c_{\mathrm{PS}}$

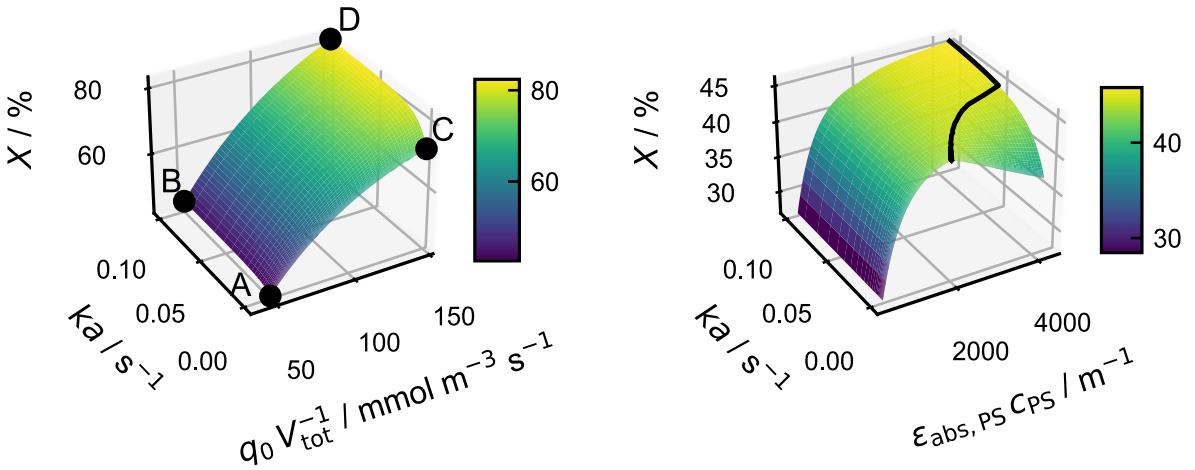

a) b)

Fig. 6: Conversion of DMA as a function of the mass transfer coefficient at β_G *= 0.5 and* $\dot{V}_{in} = 1$ mL min^{-1}. *a)* $\varepsilon_{abs,PS} c_{PS} = 2540$ m^{-1} *and varying* $q_0 V_{tot}^{-1}$, *b)* $q_0 V_{tot}^{-1} = 50$ mmol m^{-3} s^{-1} *and varying* $\varepsilon_{abs,PS} c_{PS}$. *The black line highlights the maximum conversions.*

due to a higher DMA availability in the irradiated compartment. The corresponding higher reaction rate outweighs the inhibitive effect of the shrinking irradiated volume.

To assess the impact of ka on the reactor performance, Da_I and Da_{II} can be used as indicators [35]. Da_I directly correlates with the conversion [36]. Above $Da_{II} = 1$, light attenuation leads to a heterogeneous concentration field in the radial direction and thus radial mass transport affects the reaction [35].

An investigation of Da_I and Da_{II} is shown exemplarily for experimental data at $\beta_G = 0.5$ in Fig. 7. Da_{II} exceeds 1 at $q_0 V_{tot}^{-1} \geq 93$ mmol m^{-3} s^{-1} and $\varepsilon_{abs,PS} c_{PS} = 2540$ m^{-1}, the maximum values of both variables studied in the experiments. At the same time, the highest Da_I is reached under these conditions. Since usually a high conversion is desired, *i.e.,* a high Da_I, mass transport limitations have to be considered in many eligible operation points with a high incident photon flux and a high linear absorption coefficient.

It must be emphasized that already for the small reactor diameter of 1 mm, light attenuation and mass transport limitations may reduce the substrate conversion. The incident photon flux and the linear absorption coefficient are identified as the key parameters affecting the optimum trade-off between optical pathlength and reaction rate that lead to

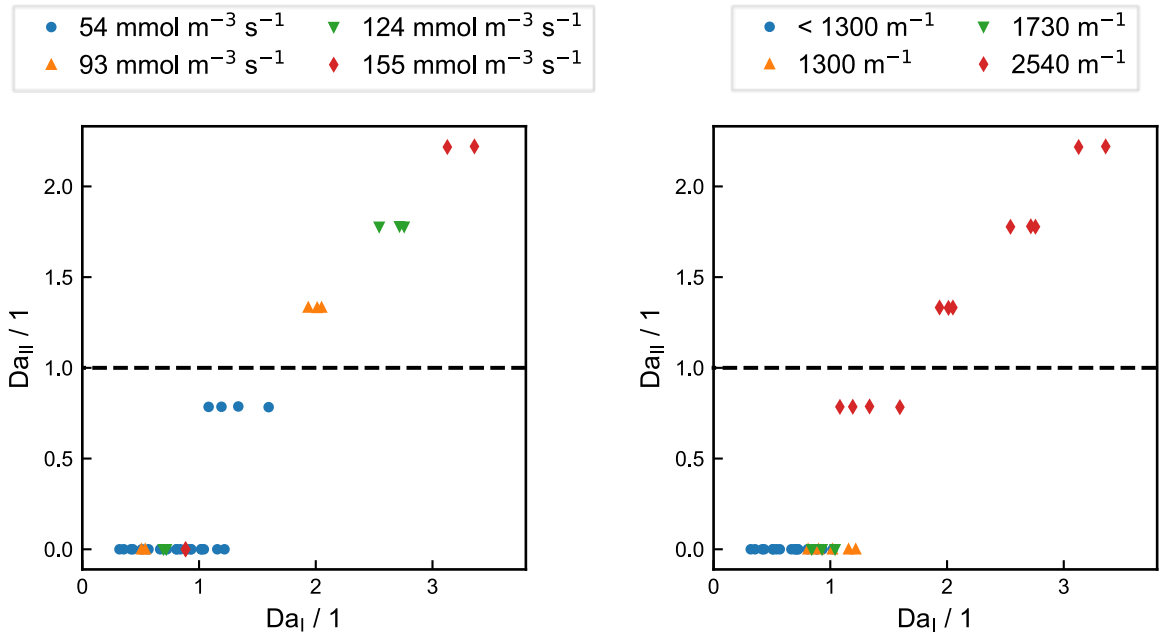

a) Sorted by $q_0\ V_{tot}^{-1}$

b) Sorted by $\varepsilon_{PS,\,abs}\ c_{PS}$

Fig. 7: Analysis of the experimental data of Roibu et al. at $\beta_G = 0.5$ by Damkoehler numbers I and II. At $Da_{II} > 1$, light attenuation leads to a heterogeneous concentration field in the radial direction[32].

the highest substrate conversion. Increasing the mass transport coefficient further improves the conversion.

Considering reactor scale-up, the choice of incident photon flux and linear absorption coefficient gains additional importance. Under the same reaction conditions, the substrate conversion may decrease with increasing capillary diameter due to an increased shaded volume compared to the irradiated volume. Fig. 8 shows the effect of a change of incident volumetric photon flux, ka-value and the linear absorption coefficient using capillary diameters of 1 mm, 2 mm, and 5 mm. The inlet flow rate is adjusted so that the residence time is equal in each case.

In Fig. 8 a), the conversion, the photonic efficiency and the intensification factor are illustrated as a function of ka with increasing volumetric photon flux from i) to iii). Independent of the reactor diameter, X and I increase with $q_0\ V_{tot}^{-1}$ due to the higher reaction rate according to equations (19) and (20). At the same time ξ decreases, since the increase in

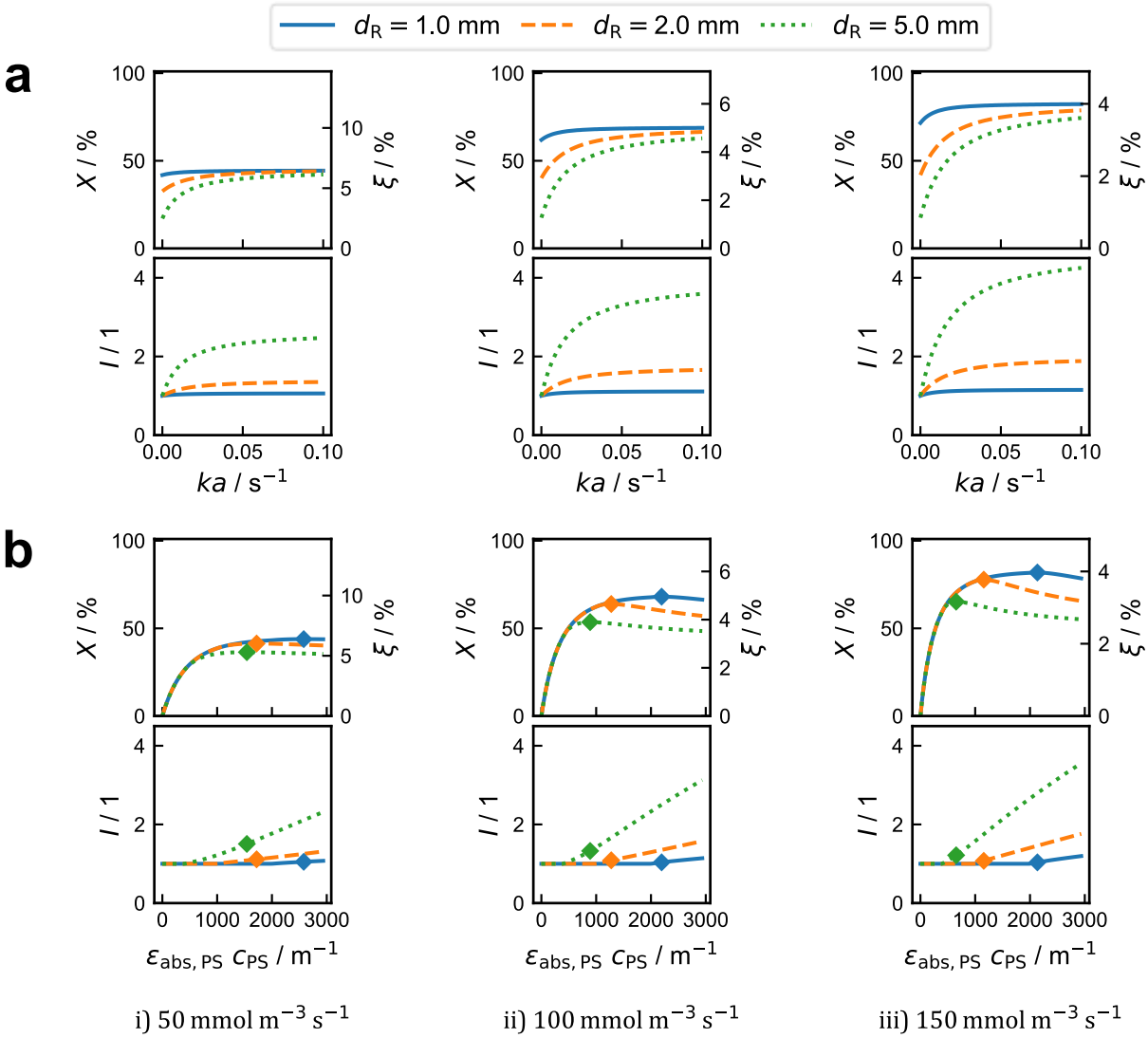

Fig. 8: Simulated conversion, photonic efficiency and intensification factor for various capillary diameters. The inlet flow rate is scaled with the diameter to ensure a comparable residence time and the incident volumetric photon flux is increased from i) to iii). a) Variation of the mass transfer coefficient between irradiated- and shaded compartment at $\varepsilon_{abs,PS} c_{PS} = 2540\ \mathrm{m}^{-1}$, *b) variation of the linear absorption coefficient at* $ka = 2.36 \cdot 10^{-2}\ \mathrm{s}^{-1}$. *The points highlight the maximum conversion.*

converted amount of substrate is smaller than the number of additionally supplied photons. At $ka = 0\ \mathrm{s}^{-1}$, the conversion in the 1 mm capillary is up to 2 times higher than in the 5 mm capillary due to a higher ratio of the irradiated- to shaded compartment volume in the 1 mm capillary. With increasing ka, the difference in conversion decreases until a similar conversion is reached independent of the reactor diameter at $ka = 0.1\ \mathrm{s}^{-1}$. The

enhanced mass transport mitigates the conversion limitations caused by the shaded compartment in which no reaction takes place. As the ratio of irradiated- to shaded volume decreases with increasing diameter, the intensification factor increases with higher diameter. In the 1 mm capillary, I equals approximately 1 independent of the reaction conditions, whereas I reaches up to a value of 4.3 in the 5 mmm capillary at $q_0\ V_{\mathrm{tot}}^{-1} = 150\ \mathrm{mmol\ m^{-3}\ s^{-1}}$ and $ka = 0.1\ \mathrm{s^{-1}}$.

Fig. 8 b) shows the conversion, the photonic efficiency and the intensification factor as function of $\varepsilon_{\mathrm{abs,PS}} c_{\mathrm{PS}}$. ka is set to a value of $2.36 \cdot 10^{-2}\ \mathrm{s^{-1}}$ that is taken from Table 2. The optimum in $\varepsilon_{\mathrm{abs,PS}} c_{\mathrm{PS}}$ shifts to smaller values both with increasing capillary diameter and with increasing incident photon flux. In the 1 mm capillary, the optimum in $\varepsilon_{\mathrm{abs,PS}} c_{\mathrm{PS}}$ is $2580\ \mathrm{m^{-1}}$ at $q_0\ V_{\mathrm{tot}}^{-1} = 50\ \mathrm{mmol\ m^{-3}\ s^{-1}}$ whereas it is $650\ \mathrm{m^{-1}}$ in the 5 mm capillary at $q_0\ V_{\mathrm{tot}}^{-1} = 150\ \mathrm{mmol\ m^{-3}\ s^{-1}}$. Since the ratio of irradiated- to shaded compartment volume decreases with increasing capillary diameter, the optimum trade-off between optical pathlength and reaction rate is reached at a smaller $\varepsilon_{\mathrm{abs,PS}} c_{\mathrm{PS}}$. An increase in $q_0\ V_{\mathrm{tot}}^{-1}$ leads to a higher reaction rate and thus $q_0\ V_{\mathrm{tot}}^{-1}$ affects the optimum as well.

The intensification factor equals 1 as long as the shading criterion in equation (7) results in $l_{\mathrm{irr}} = d_{\mathrm{R}}$, since the shaded volume is 0. Thus, no radial mass transport between the compartments occurs. When equation (7) results in $l_{\mathrm{irr}} < d_{\mathrm{R}}$, I increases approximately linearly with $\varepsilon_{\mathrm{abs,PS}} c_{\mathrm{PS}}$. The slope increases with reactor diameter, *i.e.*, in a larger diameter the impact of mass transport increases. In the 1 mm capillary, I is close to 1 at the optimum value of $\varepsilon_{\mathrm{abs,PS}} c_{\mathrm{PS}}$ and it is in the range of $1.2 - 1.5$ in case of the 5 mm capillary.

An alternative scale-up approach is shown in Fig. *9*. Instead of the volumetric photon flux, the irradiance is kept constant when the reactor diameter is increased. Such a procedure may be applied to achieve well-characterized conditions if only the irradiance of the light source is known. In case of a constant irradiance, the ratio of photons to educt decreases during scale-up. The molar amount of educt scales with reactor volume ($\propto d_{\mathrm{R}}^2$), while I_0 scales with reactor surface area ($\propto d_{\mathrm{R}}$). Due to the decreasing photon to educt ratio, the conversion decreases with increasing reactor diameter and the photonic efficiency increases. Compared to a constant incident volumetric photon flux assumed in Fig. *8*., the optimum linear absorption coefficient is higher at constant irradiance in the 2 mm and

the 5 mm capillary. Since $q_0\ V_{\mathrm{tot}}^{-1}$ is smaller at constant irradiance and thus the rate increase is smaller but the asymptotic decline of the irradiated volume remains unchanged, the ideal trade-off between reaction rate and irradiated volume is reached at a higher linear absorption coefficient.

Similar to a constant volumetric photon flux, the intensification factor increases both with increasing reactor diameter and increasing amount of incident photons. The absolute value of I, however, is generally smaller at constant irradiance, since the conversion drop during scale up is mainly governed by the reduced $q_0\ V_{\mathrm{tot}}^{-1}$ and not by internal mass transport limitations on the liquid side.

In summary, the simulations highlight the critical influence of light attenuation and mass transport constraints on the photoreactor performance, even at the laboratory scale. Optimizing the reaction conditions solely for a high conversion would lead to a decrease of the photonic efficiency by a factor of about 2 for the studied photooxygenation (1 mm vs. 5 mm capillary for low and high irradiance; s. Fig. *9*). As reactors are scaled up, these factors become even more significant due to a higher optical depth. The photonic efficiency determines the amount of electricity required for operation and thus the variable costs. Hence, scalable reactor concepts are required that provide efficient liquid mixing also at larger dimensions.

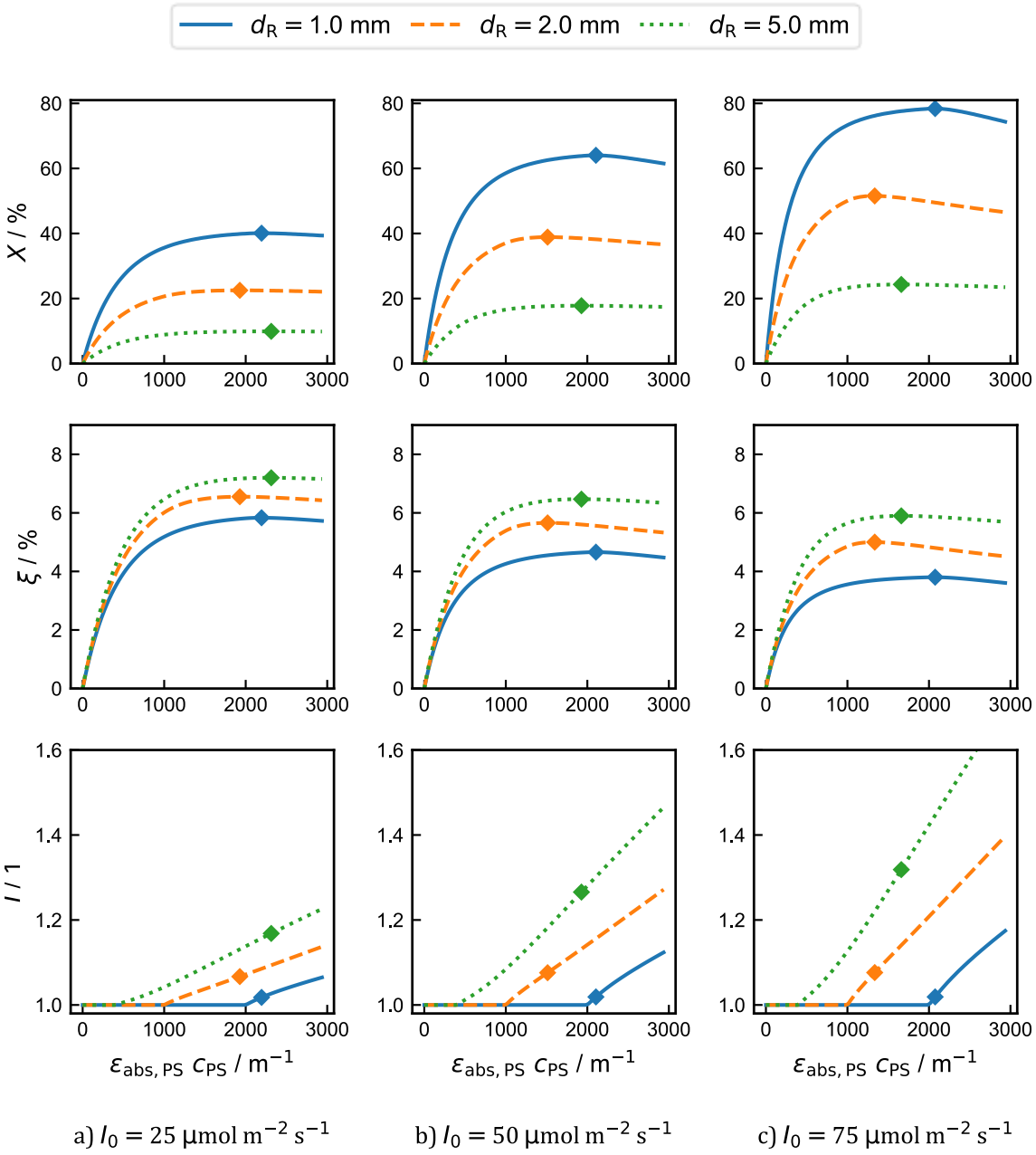

Fig. 9: Simulated conversion, photonic efficiency, and intensification factor for various capillary diameters at $ka = 2.36 \cdot 10^{-2}$ s^{-1} as a function of $\varepsilon_{abs,PS} c_{PS}$ with increasing initial light intensity from a) to c). The points highlight the maximum conversion.

285

4 Conclusion

In this work, the impact of light attenuation and mass transport limitations in the liquid phase on the performance of a photoreactor was investigated. For this purpose, a compartment model was developed and applied to a photooxidation in a Taylor-flow capillary reactor. The incident photon flux, the linear absorption coefficient and the ka-value between irradiated- and shaded compartment are shown to be crucial parameters affecting the conversion in a photoreactor.

Increasing the incident photon flux improves the substrate conversion. However, the issue of an increasing shaded volume during scale-up is not directly addressed by a change in incident photon flux. Instead, only the reaction rate in the irradiated part of the reactor is increased. The photonic efficiency decreases and thus, a sole increase in incident photon flux is not a viable option for economic reactor scale-up.

Changing the linear absorption coefficient is beneficial only as long as the increase in reaction rate outweighs the decrease in the irradiated volume in the reactor. The optimum value of $\varepsilon_{\mathrm{abs,PS}} c_{\mathrm{PS}}$ depends on the depth of the reactor and on $q_0\ V_{\mathrm{tot}}^{-1}$. During reactor scale-up, a thorough optimization of both $\varepsilon_{\mathrm{abs,PS}} c_{\mathrm{PS}}$ and $q_0\ V_{\mathrm{tot}}^{-1}$ is therefore required to design an economically viable high-performance reactor. In addition, the intensification of liquid mixing is essential to mitigate conversion limitations caused by shading, especially for large reactors.

The presented results underline the practical relevance of mass-transport enhanced photoreactors, which have been studied more intensively in recent years [37,38]. The identified mass transport limitation in the liquid phase is even more relevant for larger reaction networks, which raise selectivity challenges. Depletion of a reactant in the irradiated zone can favor the formation of by-products, ultimately limiting the applicability of higher power light sources and requiring alternative scale-up concepts. Thus, it is imperative for an efficient reactor scale-up to intensify internal mass transport within the liquid. The availability of high power light sources is key for an industrial application of photochemical processes, but requires a reevaluation of scale-up approaches with special focus on the core reaction engineering fields of heat and mass transport.

Declaration of Competing Interest

The authors declare that they have no known competing financial interests or personal relationships that could have appeared to influence the work reported in this paper.

Acknowledgement

B.W. thanks Dr. Fabian Guba and Dr. Daniel Kowalczyk from the Institute of Chemical Engineering at Ulm University as well as Dr. Anca Roibu from the Hahn-Schickard Institute, Ulm Germany, for the support and the scientific contribution during the early conceptual design phase. D.Z. thanks thanks the Deutsche Forschungsgemeinschaft for support by the collaborative research center TRR234 "CataLight" (364549901), project C6.

S.K. acknowledges funding from the Flemish Research Council (FWO) and from the European Research Council under the European Union's Horizon 2020 research and innovation programme (grant agreement No. 101001024).

Data Availability Statement

The data supporting the findings of this study are available within the paper and its Supplementary Information files.

Author Contributions

Benedikt Wiedemann: Conceptualization (equal); Data Curation (lead); Formal Analysis (lead); Investigation (lead); Methodology (lead); Software (lead); Validation (lead); Visualization (lead); Writing – Original Draft (lead); Writing – Review & Editing (equal).

Keiran Mc Carogher: Methodology (supporting); Writing – Review & Editing (supporting).

Simon Kuhn: Funding Acquisition (supporting); Supervision (supporting); Writing – Review & Editing (supporting).

Dirk Ziegenbalg: Conceptualization (equal); Funding Acquisition (lead); Methodology (supporting); Supervision (lead); Writing – Review & Editing (equal).

Appendix

A Influence of the Residence Time Distribution

Roibu et al. investigated the residence time distribution in the reactor that is used as benchmark case in this study. The determined vessel dispersion number is in the range of $3 \cdot 10^{-2}$ to $6 \cdot 10^{-2}$ under homogeneous conditions and in the range of $2 \cdot 10^{-4}$ to $6 \cdot 10^{-3}$ under Taylor-flow conditions [15]. Since a vessel dispersion number above $1 \cdot 10^{-2}$ indicates a significant deviation from plug flow behavior [39], the residence time distribution may affect the DMA conversion under homogeneous conditions.

To investigate the influence of the residence time distribution, laminar flow behavior is assumed, which is typical for microreactors [40,41]. The resulting parabolic liquid velocity profile $u_\mathrm{l}(x)$ is illustrated schematically in Fig. A1 a). It can be expressed by equation (A.1), $x = 0$ is chosen as the reactor surface closest to the light source.

$$u_\mathrm{l}(x) = u_\mathrm{l,max}\left(1 - \frac{\left(x - \frac{d_\mathrm{R}}{2}\right)^2}{\left(\frac{d_\mathrm{R}}{2}\right)^2}\right) \tag{A.1}$$

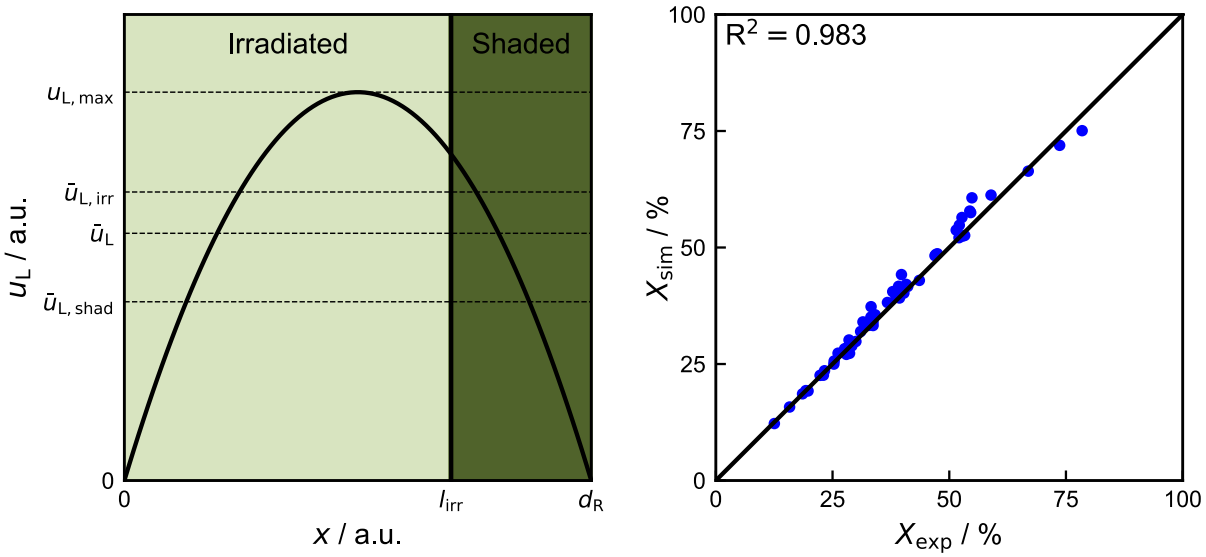

Fig. A1: Influence of the residence time distribution on the DMA conversion in the benchmark reactor. a) Schematic overview of the velocity in the irradiated- and in the shaded compartment due to the laminar velocity profile. b) Comparison of experimental data reported by Roibu et al.[14] and the simulated conversion based on a laminar velocity profile.

355 $u_{\mathrm{l,max}}$ is the maximum liquid velocity in the center of the reactor. Considering the overall
356 mass balance, equation (A.2) must be satisfied for the mean liquid velocity $\bar{u}_{\mathrm{l}}$. Therefore,
357 $u_{\mathrm{l,max}}$ can be determined by equation (A.3).

$$\bar{u}_{\mathrm{l}} = \frac{1}{d_{\mathrm{R}}} \int_0^{d_{\mathrm{R}}} u(x)\,\mathrm{d}x = \frac{\dot{V}_{\mathrm{in}}}{A_{\mathrm{cross}}} \tag{A.2}$$

$$u_{\mathrm{l,max}} = \frac{\dot{V}_{\mathrm{in}}}{A_{\mathrm{cross}}} \cdot d_{\mathrm{R}} \cdot \left[\int_0^{d_{\mathrm{R}}} \left(1 - \frac{\left(x - \frac{d_{\mathrm{R}}}{2}\right)^2}{\left(\frac{d_{\mathrm{R}}}{2}\right)^2} \right) \mathrm{d}x \right]^{-1} \tag{A.3}$$

358 Due to the parabolic velocity profile, the mean velocities in the irradiated- and in the
359 shaded compartment $\bar{u}_{\mathrm{l,irr}}$ and $\bar{u}_{\mathrm{l,shad}}$ depend on the optical pathlength according to equa-
360 tions (A.4) and (A.5).

$$\bar{u}_{\mathrm{l,irr}} = \frac{1}{l_{\mathrm{irr}}} \int_0^{l_{\mathrm{irr}}} u(x)\,\mathrm{d}x \tag{A.4}$$

$$\bar{u}_{\mathrm{l,shad}} = \frac{1}{d_{\mathrm{R}} - l_{\mathrm{irr}}} \int_{l_{\mathrm{irr}}}^{d_{\mathrm{R}}} u(x)\,\mathrm{d}x \tag{A.5}$$

361 Using the same derivation approach as in section 2.1 results in the balance equations (A.6)
362 and (A.7).

$$-\bar{u}_{\mathrm{l,irr}} \frac{\mathrm{d}c_{\mathrm{irr}}}{\mathrm{d}z} + ka(c_{\mathrm{shad}} - c_{\mathrm{irr}}) \cdot \frac{\mathrm{d}V}{\mathrm{d}V_{\mathrm{irr}}} - r_{\mathrm{irr}} = 0 \tag{A.6}$$

$$-\bar{u}_{\mathrm{l,shad}} \frac{\mathrm{d}c_{\mathrm{shad}}}{\mathrm{d}z} - ka(c_{\mathrm{shad}} - c_{\mathrm{irr}}) \cdot \frac{\mathrm{d}V}{\mathrm{d}V_{\mathrm{shad}}} = 0 \tag{A.7}$$

363 Fig. A1 b) shows a comparison of the experimental DMA conversion under homogeneous
364 conditions and the simulation results based on equations (A.6) and (A.7). The R^2-value
365 equals 98.3% compared to 97.2% using the model described in section 2.1. Therefore, the
366 residence time distribution influences the DMA conversion in the investigated reactor.
367 However, the simplifying assumption of plug flow behavior still allows a good prediction,
368 given the small deviation in the R^2-values.

369

B Validation of the shading criterion

The shading criterion defined in equation (7) is validated based on the homogeneous conditions within the experimental data of the DMA conversion, since no G-L interactions need to be considered there. In addition, no mass transfer between the shaded and the irradiated compartment is assumed.

Fig. B1 shows the R^2-value of the predicted conversions by the homogeneous model compared to the experimental conversions. As indicated by the red line, R^2 is close to its maximum value. Therefore, it is reasonable to use the optical pathlength at which 1% of the initial light intensity is reached to distinguish between the irradiated- and the shaded compartment of the reactor.

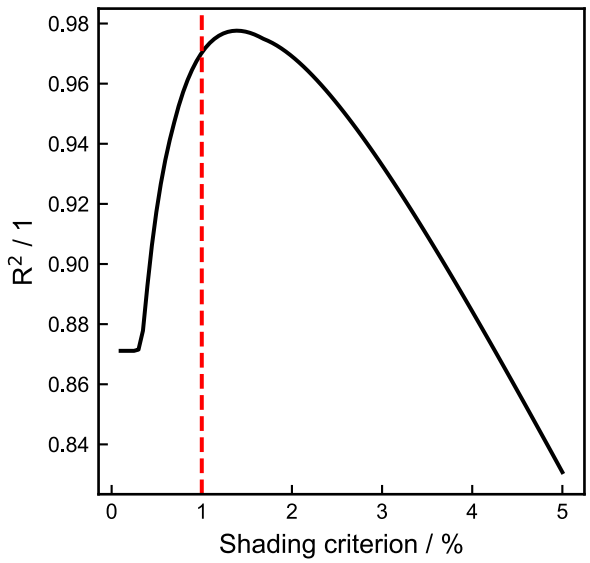

Fig. B1: R^2-value of the predicted conversions by the homogeneous model compared to the experimental conversions, plotted against shading criterion used in the homogeneous model. The red line indicates 1 % which is used in all simulations.

References

[1] Energy Institute, Statistical Review of World Energy - with major processing by Our World in Data, 2023. https://ourworldindata.org/grapher/primary-energy-source-bar (accessed 29 April 2024).

[2] Statista, Prognose zum weltweiten Primärenergieverbrauch bis zum Jahr 2050, 2021. https://de.statista.com/statistik/daten/studie/28941/umfrage/prognose-zum-energieverbrauch-weltweit-betrachtet-von-1980-bis-2030 (accessed 29 October 2023).

[3] IEA, Greenhouse Gas Emissions from Energy Data Explorer – Data Tools, 2023. https://www.iea.org/data-and-statistics/data-tools/greenhouse-gas-emissions-from-energy-data-explorer (accessed 29 October 2023).

[4] B.M. Hunter, H.B. Gray, A.M. Müller, Earth-Abundant Heterogeneous Water Oxidation Catalysts, Chemical Reviews 116 (2016) 14120–14136. https://doi.org/10.1021/acs.chemrev.6b00398.

[5] E. Kayahan, M. Jacobs, L. Braeken, L.C. Thomassen, S. Kuhn, T. van Gerven, M.E. Leblebici, Dawn of a new era in industrial photochemistry: the scale-up of micro- and mesostructured photoreactors, Beilstein J. Org. Chem. 16 (2020) 2484–2504. https://doi.org/10.3762/bjoc.16.202.

[6] F. Guba, Ü. Tastan, K. Gugeler, M. Buntrock, T. Rommel, D. Ziegenbalg, Rapid Prototyping for Photochemical Reaction Engineering, Chemie Ingenieur Technik (2018). https://doi.org/10.1002/cite.201800035.

[7] J.G.H. Hermens, M.L. Lepage, A. Kloekhorst, E. Keller, R. Bloem, M. Meijer, B.L. Feringa, Development of a modular photoreactor for the upscaling of continuous flow photochemistry, React. Chem. Eng. 7 (2022) 2280–2284. https://doi.org/10.1039/d2re00310d.

[8] A. Chaudhuri, S.D.A. Zondag, J.H.A. Schuurmans, J. van der Schaaf, T. Noël, Scale-Up of a Heterogeneous Photocatalytic Degradation Using a Photochemical Rotor-Stator Spinning Disk Reactor, Org. Process Res. Dev. 26 (2022) 1279–1288. https://doi.org/10.1021/acs.oprd.2c00012.

[9] D.S. Lee, M. Sharabi, R. Jefferson-Loveday, S.J. Pickering, M. Poliakoff, M.W. George, Scalable Continuous Vortex Reactor for Gram to Kilo Scale for UV and Visible Photochemistry, Org. Process Res. Dev. 24 (2020) 201–206. https://doi.org/10.1021/acs.oprd.9b00475.

[10] S. Naskar, D. Kowalczyk, S. Mal, S. Das, D. Mandal, P. Kumar, D. Ziegenbalg, Making photochemistry scalable – an operationally simple falling film looping photoreactor, React. Chem. Eng. 8 (2023) 2211–2222. https://doi.org/10.1039/D3RE00107E.

[11] D. Ziegenbalg, F. Gaulhofer, M. Metzger, A. Peschl, Enhancing mass transport to accelerate photoreactions and enable scale-up, React. Chem. Eng. (2024). https://doi.org/10.1039/D3RE00689A.

[12] K. Terao, Y. Nishiyama, K. Kakiuchi, Highly Efficient Asymmetric Paternò–Büchi Reaction in a Microcapillary Reactor Utilizing Slug Flow, J Flow Chem 4 (2015) 35–39. https://doi.org/10.1556/JFC-D-13-00035.

[13] M. Nakano, Y. Nishiyama, H. Tanimoto, T. Morimoto, K. Kakiuchi, Remarkable Improvement of Organic Photoreaction Efficiency in the Flow Microreactor by the Slug Flow Condition Using Water, Org. Process Res. Dev. 20 (2016) 1626–1632. https://doi.org/10.1021/acs.oprd.6b00181.

[14] R. Telmesani, J.A.H. White, A.B. Beeler, Liquid-Liquid Slug-Flow-Accelerated [2+2] Photocycloaddition of Cinnamates, ChemPhotoChem 2 (2018) 865–869. https://doi.org/10.1002/cptc.201800081.

[15] A. Roibu, T. van Gerven, S. Kuhn, Photon Transport and Hydrodynamics in Gas-Liquid Flows Part 1: Characterization of Taylor Flow in a Photo Microreactor, ChemPhotoChem 4 (2020) 5181–5192. https://doi.org/10.1002/cptc.202000065.

[16] A. Roibu, K. Mc Carogher, R.B. Morthala, R. Eyckens, S. Kuhn, Modelling approaches to predict light absorption in gas-liquid flow photosensitized oxidations, Chemical Engineering Journal 452 (2023) 139272. https://doi.org/10.1016/j.cej.2022.139272.

[17] T. Horie, M. Sumino, T. Tanaka, Y. Matsushita, T. Ichimura, J. Yoshida, Photodimerization of Maleic Anhydride in a Microreactor Without Clogging, Org. Process Res. Dev. 14 (2010) 405–410. https://doi.org/10.1021/op900306z.

[18] G. Morrison, R. Bannon, S. Wharry, T.S. Moody, N. Mase, M. Hattori, H. Manyar, M. Smyth, Continuous flow photooxidation of alkyl benzenes using fine bubbles for

mass transfer enhancement, Tetrahedron Letters 90 (2022) 153613. https://doi.org/10.1016/j.tetlet.2021.153613.

[19] M.T. Kreutzer, P. Du, J.J. Heiszwolf, F. Kapteijn, J.A. Moulijn, Mass transfer characteristics of three-phase monolith reactors, Chemical Engineering Science 56 (2001) 6015–6023. https://doi.org/10.1016/S0009-2509(01)00271-8.

[20] M.T. Kreutzer, F. Kapteijn, J.A. Moulijn, J.J. Heiszwolf, Multiphase monolith reactors: Chemical reaction engineering of segmented flow in microchannels, Chemical Engineering Science 60 (2005) 5895–5916. https://doi.org/10.1016/j.ces.2005.03.022.

[21] C. Mendoza, N. Emmanuel, C.A. Páez, L. Dreesen, J.-C.M. Monbaliu, B. Heinrichs, Transitioning from conventional batch to microfluidic processes for the efficient singlet oxygen photooxygenation of methionine, Journal of Photochemistry and Photobiology A: Chemistry 356 (2018) 193–200. https://doi.org/10.1016/j.jphotochem.2017.12.028.

[22] C. Sambiagio, T. Noël, Flow Photochemistry: Shine Some Light on Those Tubes!, Trends in Chemistry 2 (2020) 92–106. https://doi.org/10.1016/j.trechm.2019.09.003.

[23] M. Lancel, C. Gomez, M. Port, Z. Amara, 2021. Performances of Homogeneous and Heterogenized Methylene Blue on Silica Under Red Light in Batch and Continuous Flow Photochemical Reactors. Front. Chem. Eng. 3, 752364. https://doi.org/10.3389/fceng.2021.752364.

[24] I. Pibiri, S. Buscemi, A. Palumbo Piccionello, A. Pace, Photochemically Produced Singlet Oxygen: Applications and Perspectives, ChemPhotoChem 2 (2018) 535–547. https://doi.org/10.1002/cptc.201800076.

[25] M. Le Bechec, N. Costarramone, T. Pigot, S. Lacombe, Gas-Phase Photooxidation: Reactors and Materials, Chem. Eng. Technol. 39 (2016) 26–38. https://doi.org/10.1002/ceat.201500349.

[26] J. Yue, G. Chen, Q. Yuan, L. Luo, Y. Gonthier, Hydrodynamics and mass transfer characteristics in gas–liquid flow through a rectangular microchannel, Chemical Engineering Science 62 (2007) 2096–2108. https://doi.org/10.1016/j.ces.2006.12.057.

[27] M.A. Woldesemayat, Comparison of Void Fraction Correlations for Two-Phase Flow in Horizontal and Upward Inclined Flows.

[28] A. Zeghloul, A. Messilem, N. Ghendour, A. Al-Sarkhi, A. Azzi, A. Hasan, Theoretical study and experimental measurement of the gas liquid two-phase flow through a vertical Venturi meter, Proceedings of the Institution of Mechanical Engineers, Part C: Journal of Mechanical Engineering Science 235 (2021) 1567–1584. https://doi.org/10.1177/0954406220947118.
[29] J.R.S. Thom, Prediction of pressure drop during forced circulation boiling of water, International Journal of Heat and Mass Transfer 7 (1964) 709–724. https://doi.org/10.1016/0017-9310(64)90002-x.
[30] D. Chisholm, Two-phase flow in heat exchangers, Longman Higher Education, Harlow, England, 1983.
[31] T. Sato, Y. Hamada, M. Sumikawa, S. Araki, H. Yamamoto, Solubility of Oxygen in Organic Solvents and Calculation of the Hansen Solubility Parameters of Oxygen, Ind. Eng. Chem. Res. 53 (2014) 19331–19337. https://doi.org/10.1021/ie502386t.
[32] Y. Usui, M. Tsukada, H. Nakamura, Kinetic Studies of Photosensitized Oxygenation by Singlet Oxygen in Aqueous Micellar Solutions, BCSJ 51 (1978) 379–384. https://doi.org/10.1246/bcsj.51.379.
[33] E. Hairer, G. Wanner, Solving Ordinary Differential Equations II, Springer Berlin Heidelberg, Berlin, Heidelberg, 1991.
[34] M. Sender, D. Ziegenbalg, Radiometric measurement techniques for in-depth characterization of photoreactors – part 2: 3 dimensional and integral radiometry, React. Chem. Eng. 6 (2021) 1614–1627. https://doi.org/10.1039/d0re00457j.
[35] T. Aillet, K. Loubière, L. Prat, O. Dechy-Cabaret, Impact of the diffusion limitation in microphotoreactors, AIChE Journal 61 (2015) 1284–1299. https://doi.org/10.1002/aic.14718.
[36] H.S. Fogler, Elements of chemical reaction engineering, fourthth ed., Prentice Hall PTR, Upper Saddle River, NJ, 2005.
[37] F. Gaulhofer, H. Becker, A. Peschl, D. Ziegenbalg, Modelling the Impact of Mass Transport in a Miniplant Photoreactor, 2024.
[38] B. Vandekerckhove, B. Ruttens, B. Metten, C. Stevens, T. Heugebaert, Continuous Flow Scale-Up of Enantiospecific Solid-to-Solid Photodecarbonylation Chemistry Through Pulsed Flow Operation and Inline Crystallization, 2024.

505 [39] O. Levenspiel, Chemical reaction engineering, third. ed., Wiley, New York [u.a.],
506 1999.
507 [40] S.K.R. Cherlo, S. K., P. S., Screening, Selecting, and Designing Microreactors, Ind. Eng.
508 Chem. Res. 48 (2009) 8678–8684. https://doi.org/10.1021/ie900306j.
509 [41] A.A. Bojang, H.-S. Wu, Design, Fundamental Principles of Fabrication and Applica-
510 tions of Microreactors, Processes 8 (2020) 891.
511 https://doi.org/10.3390/pr8080891.